PHOTONICS Research

Design of a micrometer-long superconducting nanowire perfect absorber for efficient high-speed single-photon detection

Risheng Cheng,[1] Sihao Wang,[1] Chang-Ling Zou,[1,2] and Hong X. Tang[1,*]

[1]Department of Electrical Engineering, Yale University, New Haven, Connecticut 06511, USA
[2]Department of Optics, University of Science and Technology of China, Hefei 230026, China
*Corresponding author: hong.tang@yale.edu

Received 20 February 2020; revised 27 May 2020; accepted 2 June 2020; posted 3 June 2020 (Doc. ID 390945); published 14 July 2020

Despite very efficient superconducting nanowire single-photon detectors (SNSPDs) reported recently, combining their other performance advantages such as high speed and ultralow timing jitter in a single device still remains challenging. In this work, we present a perfect absorber model and the corresponding detector design based on a micrometer-long NbN nanowire integrated with a 2D photonic crystal cavity of ultrasmall mode volume, which promises simultaneous achievement of near-unity absorption, gigahertz counting rates, and broadband optical response with a 3 dB bandwidth of 71 nm. Compared to previous stand-alone meandered and waveguide-integrated SNSPDs, this perfect absorber design addresses the trade space in size, efficiency, speed, and bandwidth for realizing large on-chip single-photon detector arrays.

https://doi.org/10.1364/PRJ.390945

1. INTRODUCTION

Superconducting nanowire single-photon detectors (SNSPDs) [1,2] are recognized as one of the most important photon detection technologies in quantum information processing and communications [3–5], due to their high internal quantum efficiency over a broad wavelength band [6–11], fast speed [12,13], excellent timing performance [14–16], and ultralow dark count rates [17,18]. However, these individual performance characteristics have so far been best optimized in separate device designs, and it still remains a challenge to incorporate all the high-performance merits in a single device, due to the inherent trade-off between detection efficiency and bandwidth over a desired nanowire length. For example, in most high-efficiency SNSPD designs, it is preferable that the devices consist of an ultrathin and millimeter-long superconducting nanowire meandered into a circular shape with >15 μm diameter to guarantee near-unity coupling efficiency from fiber to detector [6–8,19], which renders the detectors subject to speed limited by the large kinetic inductance of the long nanowires [20]. Integrating the nanowire detectors with on-chip optical waveguides could greatly increase the interaction time of the nanowire with photons and thereby reduce the absorption length of the nanowire down to tens of micrometers [21–31]. Nevertheless, the total length of the nanowire needs further scale down below 10 μm in order to realize gigahertz counting rates [32]. Moreover, the SNSPD with a record-low timing jitter below 3 ps has only been demonstrated with a 5 μm-long NbN nanowire recently [16] in order to suppress the geometry-induced jitter [33], albeit with a compromised detection efficiency due to direct free-space illumination. Considerable efforts have been devoted to further reducing the nanowire length by embedding the nanowires into a variety of cavities, such as 1D and 2D photonic crystal (PhC) cavities [12,32,34] and racetrack ring resonators [35]. While as short as 1 μm-long nanowires have been demonstrated with considerable absorption, the use of resonant cavities introduces spectral selectivity, resulting in an operation bandwidth of only several nanometers.

The main goal of this work is to design a near-perfect absorber for an ultrashort nanowire of 1 μm in length, while simultaneously maintaining a broad operation bandwidth around the telecommunication wavelength of 1550 nm. We begin by theoretically studying a general one-side cavity model in Section 2 to guide the optimization of the nanowire-loaded cavity system. Then, we systematically investigate the absorption rates of the waveguide-integrated NbN nanowires in dependence on the index contrast of waveguides, nanowire geometry, and varying waveguide types to maximize the photon loss per round trip in the cavity (Section 3). In Section 4, we present the design and simulation results of the ultrashort NbN nanowire integrated with an H0-type 2D-PhC cavity, which demonstrates an ultrasmall mode volume and thus enables the nanowire to achieve a near-unity peak absorption efficiency, combined with more than 70 nm 3 dB bandwidth maintained. In Section 5, we compare our design with previous

implementations of SNSPDs based on different device structures, and the results demonstrate orders of magnitude improvement achieved with our design in terms of the bandwidth-nanowire-length ratio, which holds promise for realizing a large array of high-performance on-chip single-photon detectors for future integrated quantum photonic circuits.

2. ONE-SIDE CAVITY MODEL

In order to study the effect of the cavity on the nanowire absorption bandwidth, we propose a simple and general one-side cavity model, as illustrated in Fig. 1(a). The nanowire is placed inside a cavity that is formed by a fully reflective mirror combined with another partially reflective mirror. Through the partial mirror, light could couple into and out of the cavity with the designed coupling coefficient κ, while r denotes the field amplitude reflection coefficient of the partial mirror. We assume there is no loss in the coupling region, and thus the relation $r^2 + \kappa^2 = 1$ holds. Using the transfer-matrix method [36], we could relate the fields at the left and right side of the partial mirror as

$$\begin{bmatrix} a_{\text{in}} \\ a_{\text{out}} \end{bmatrix} = \frac{1}{\kappa}\begin{bmatrix} 1 & r \\ r & 1 \end{bmatrix}\begin{bmatrix} b_1 \\ b_2 \end{bmatrix}, \tag{1}$$

where a_{in} and a_{out} represent the incident field and the reflected field from the cavity, while b_1 and b_2 denote the field inside the cavity propagating forward and backward, respectively. b_1 and b_2 are further related by

$$b_2 = b_1 \alpha e^{-i\theta}, \tag{2}$$

and

$$\theta = 4\pi L n_{\text{eff}}/\lambda + \pi, \tag{3}$$

where α, θ, L, n_{eff}, and λ represent the amplitude attenuation coefficient, the round-trip phase shift, the cavity length, the effective index of the cavity, and the wavelength of the incident light, respectively. By substituting Eqs. (2) and (3) into Eq. (1), we obtain the power absorption efficiency A and the reflectance of the cavity R as follows:

$$\begin{aligned} A &= 1 - R \\ &= 1 - \left|\frac{a_{\text{out}}}{a_{\text{in}}}\right|^2 \\ &= 1 - \left|\frac{r + \alpha e^{-i\theta}}{1 + r\alpha e^{-i\theta}}\right|^2 \\ &= 1 - \frac{r^2 + \alpha^2 - 2r\alpha\cos\theta}{1 + (r\alpha)^2 - 2r\alpha\cos\theta}. \end{aligned} \tag{4}$$

In order to achieve perfect absorption $A = 1$, Eq. (4) indicates that two conditions must be fulfilled. (1) The cavity needs to be on resonance, i.e., $\lambda = \lambda_{\text{res}} = 4n_{\text{eff}}L/m$ or $L = m/4(\lambda_{\text{res}}/n_{\text{eff}})$, where m is the longitudinal mode order number and has to be a positive integer. (2) The critical coupling condition [37] should be satisfied, i.e., $r = \alpha$ for odd m and $r = -\alpha$ for even m. The negative value of r indicates half-wave loss induced at the interface between the input medium and the cavity. This condition also leads to $1 - \alpha^2 = \kappa^2$, suggesting that the coupled power into the cavity is equal to the loss. We note that α^2 mentioned here stands for the total loss of the photons per round trip in the cavity, including the desired absorption by the nanowire as well as the intrinsic loss in the cavity due to dielectric loss, scattering, and radiation. Therefore, the designed cavity should have negligible intrinsic loss compared to the nanowire absorption to guarantee all the photons coupled into the cavity are ultimately absorbed by the nanowire.

From Eq. (4), we could derive the loaded quality factor Q_l and the absorption bandwidth defined as the full width at half-maximum (FWHM) of the resonance spectrum,

$$\begin{aligned} Q_l &= \frac{\lambda_{\text{res}}}{\text{FWHM}} \\ &= \frac{2\pi n_{\text{eff}} L\sqrt{|r|\alpha}}{\lambda_{\text{res}}(1 - |r|\alpha)} \\ &= \frac{m\pi\sqrt{|r|\alpha}}{2(1 - |r|\alpha)}, \end{aligned} \tag{5}$$

which can be further simplified at the condition of critical coupling ($|r| = \alpha$) as

$$Q_{l,c} = \frac{m\pi\alpha}{2(1 - \alpha^2)}. \tag{6}$$

Equation (6) suggests that in order to realize a broadband absorber with a large FWHM, Q_l should be minimized, which can be achieved by simultaneously employing a cavity of small mode volume (smaller m or L) and enhancing the absorption efficiency of photons per round trip in the cavity (smaller α). These results are further quantitatively visualized by plotting the calculated nanowire absorption spectrum for varying α and L in Figs. 1(b) and 1(c), respectively. We ignore any intrinsic loss in the cavity and assume all the photon loss is due to the absorption by the nanowire. In Fig. 1(b), we observe a significant absorption bandwidth (>200 nm) with the nanowire absorption rate $\alpha^2 = -1$ dB, which can be easily obtained

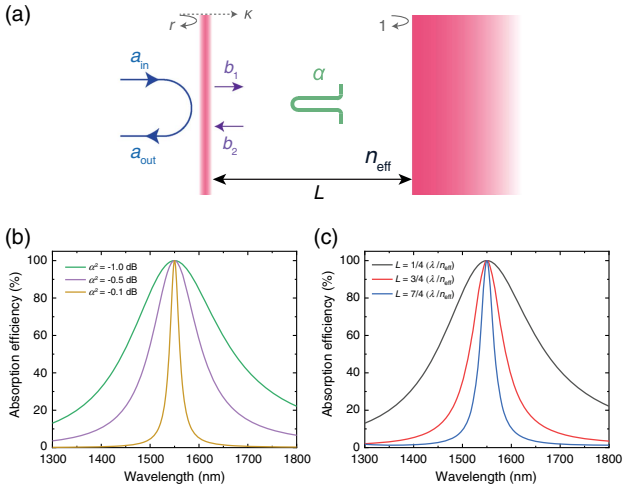

Fig. 1. One-side cavity model and calculated absorption efficiency of the nanowire absorber. (a) Schematic of the lossy cavity with an embedded nanowire absorber; (b) calculated nanowire absorption spectrum for varying photon loss per round trip in the cavity. The cavity length is fixed at $L = 1/4(\lambda/n_{\text{eff}})$. (c) Calculated nanowire absorption spectrum for varying cavity length. The photon loss per round trip is fixed at $\alpha^2 = -1.0$ dB.

by NbN nanowires atop optimized high-index waveguides at micrometer-length scale, as will be shown in Section 3. Figure 1(c) demonstrates that the FWHM decreases sharply as the mode number m increases, and thus the fundamental mode ($m = 1$) is desired for the largest bandwidth. This can explain the broadband nature of the meander-type SNSPDs with vertically integrated quarter-λ cavities [6–8,38], despite the fact that the minimum length of the nanowire is limited in another dimension. However, for on-chip integrated cavities, it is challenging to design a cavity with an extremely small mode volume combining low intrinsic loss due to the strong radiation and scattering of photons at optical frequencies. For example, to maintain an acceptable radiation loss due to waveguide bending, m is typically designed larger than 20 for microring resonators fabricated on the silicon-on-insulator (SOI) platform [39] and even larger for other medium-index waveguide platforms [40,41]. Fortunately, the advent of PhC nanocavities [42,43] provides us with the possibility of trapping light in a smaller-than-wavelength mode volume by inhibiting radiation via photonic bandgap effect, which will be further discussed in Section 4.

3. STUDY OF NANOWIRE ABSORPTION RATES

A. High-Index-Contrast and Medium-Index-Contrast Waveguides

In this subsection, we first compare the absorption rates of NbN nanowires integrated with waveguides of different index contrasts. As shown in the schematic drawings of Figs. 2(a) and 2(b), we set the index of the core material as 3.45 and 2.0 for high- and medium-index-contrast (HIC and MIC) waveguides, respectively. The waveguides have the bottom cladding of 1.45 index and air upper cladding. The MIC waveguide could approximately represent a wide range of waveguide platforms, such as SiN [23,26], GaN [44], AlN [40,45], diamond [27], and $LiNbO_3$ [46,47] on insulators (SiO_2), while GaAs [48] and Si [22] on insulators could be good examples of HIC waveguides. The U-shaped NbN nanowire is placed atop these waveguides, both as absorber and detector, via evanescent coupling to the optical mode confined in the waveguides. The complex refractive index of NbN we use in the simulation is $5.23 + i5.82$ measured by ellipsometry [49]. The thickness, width, and gap of the nanowire are set to 5, 80, and 120 nm, respectively, based on previous experimental results [7,8,50], which could guarantee saturated internal efficiency at 1550 nm wavelength.

By numerically solving the fundamental eigenmode of the waveguide, we extract the effective index of the propagating mode, the imaginary part of the effective index corresponds to the absorption. The nanowire absorption rates can be obtained using the expression $AR = 4.34(4\pi k_{\text{eff}}/\lambda)$ in units of dB/μm, where k_{eff} is the imaginary part of the effective index. We only consider fundamental TE modes in this subsection, since TE modes are more widely used in the PhC cavity design because their photonic bandgaps are larger than those of TM modes.

Figures 2(c) and 2(d) plot the simulated results of the nanowire absorption rates as a function of the waveguide width for varying MIC and HIC waveguide thickness. For both waveguide designs, the absorption rates show smooth dependence on the waveguide width, and the maximum peaks shift towards smaller width for increased waveguide thickness. For wider and thicker waveguides, the absorption rates decrease due to better confined optical mode and thus weaker evanescent coupling to the nanowire. On the other hand, the absorption rates also drop for narrower and thinner waveguides because of increased mode size and the cut-off condition. As a result, the maximum absorption rate of 0.27 dB/μm is achieved with a 300 nm-thick and 1 μm-wide MIC waveguide. For HIC waveguides, we observe almost 1 order of magnitude enhanced value of 2.3 dB/μm occurring around 100 nm thickness and 550 nm width. This huge difference is not surprising, considering a more compact mode profile is achieved with HIC waveguides in comparison with MIC waveguides, as shown in Figs. 2(a) and 2(b). The simulation results are also in good agreement with previously reported experimental values [22–24,26]. Therefore, we only focus on the optimization of HIC waveguide design in the following subsections.

B. Effect of Nanowire Geometry

In Fig. 3, we show the effect of the nanowire geometry on its absorption rates. We use the optimized HIC waveguide design shown in Fig. 2(b) with 100 nm thickness and 550 nm width. The gap between the nanowires is kept 1.5 times the width of the nanowire to relieve the current crowding

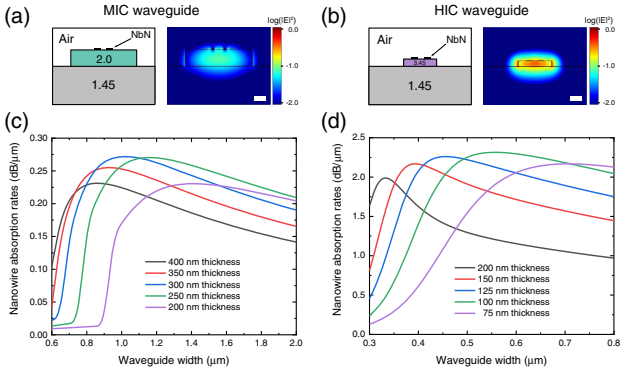

Fig. 2. Comparison between HIC and MIC waveguides. Cross-sectional schematics and simulated mode profiles of (a) MIC and (b) HIC waveguides. Scale bars, 200 nm; simulated nanowire absorption rates as a function of waveguide width for (c) MIC and (d) HIC waveguides of varying thicknesses.

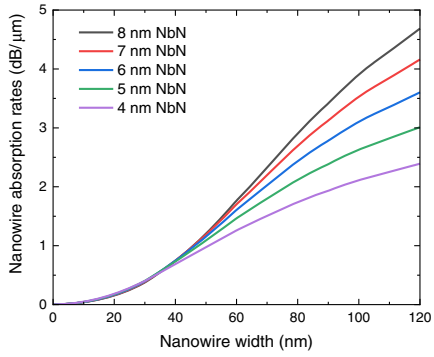

Fig. 3. Simulated nanowire absorption rates depending on the nanowire width and thickness for the optimized HIC waveguide design.

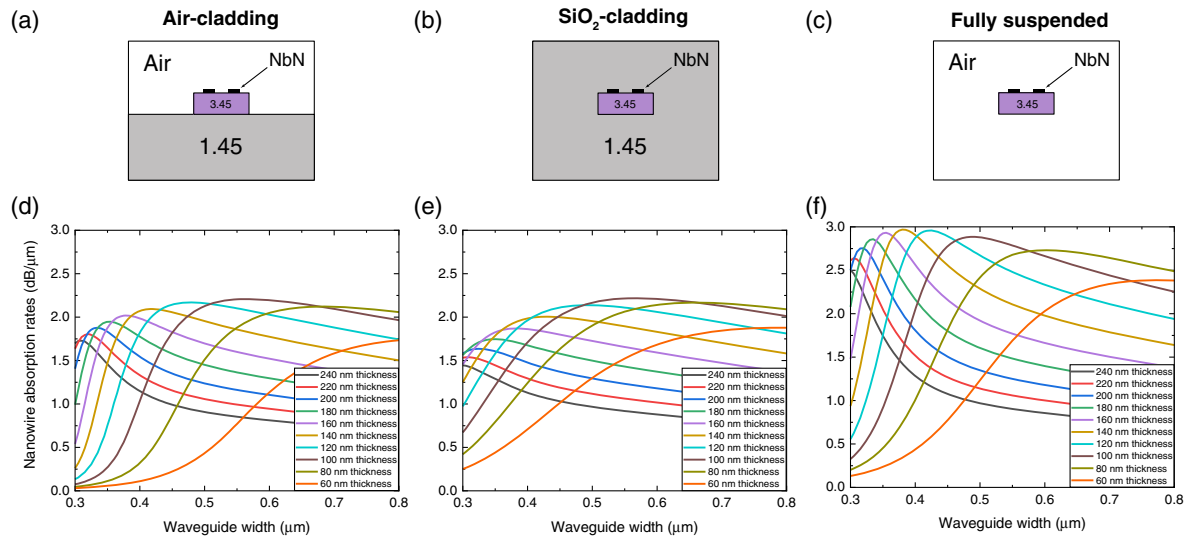

Fig. 4. Effect of the waveguide types and geometry on the nanowire absorption rates. Cross-sectional schematics of (a) air-cladding waveguide on SiO_2, (b) SiO_2-cladding buried waveguide, and (c) fully suspended waveguide. (d)–(i) Simulated nanowire absorption rates depending on the waveguide geometry for HIC waveguides with various upper and bottom claddings of different indices. The corresponding simulation results are shown in the same column as the schematics of the waveguides.

effect [51]. Interestingly, we observe that the absorption rates are nearly independent of the nanowire thickness in ultranarrow (<40 nm width) region and start to grow rapidly for larger width beyond this region. We attribute this behavior to the limited penetration of the perpendicularly polarized electric field into the ultranarrow nanowires, and similar features have also been captured and utilized in meander-type SNSPDs before [49,52]. The absorption rates tend to saturate with further increased nanowire width (>100 nm) due to displaced nanowire position from the center of the waveguide, where the evanescent field is the strongest. Based on these results, we choose a slightly wider 80 nm-width nanowire of 5 nm thickness in the following discussions, allowing for better electric field penetration into the nanowire while the nanowire is still narrow and thin enough for obtaining saturated internal efficiencies at the wavelength of 1550 nm [7,8,53].

C. Effect of Waveguide Parameters

In this subsection, we continue to investigate the absorption rates of the nanowire integrated with waveguides of various types. Following the results of previous sections, we focus on high-index waveguide core material but change the index of the upper and bottom claddings, as shown in Figs. 4(a)–4(c), which, respectively, represent the air-cladding waveguide on SiO_2, SiO_2-cladding-buried waveguide, and fully suspended waveguide. Here, we only consider fundamental TE modes, since higher-order modes provide substantially reduced absorption rates due to larger mode size. Likewise, we do not show the results of partially etched rib waveguides, which have lower absorption rates compared with ridge waveguides because of their larger and pulled-down mode profile [24]. Figures 4(d)–4(f) demonstrate simulated NbN nanowire absorption rates versus waveguide width for varying waveguide types and thicknesses. The highest absorption rates are obtained with fairly thin waveguides of 100–140 nm thickness, which could provide a strong evanescent field to couple with the nanowire. In comparison with the other two types of waveguides, the fully suspended waveguide [Fig. 4(f)] shows significantly stronger absorption for a wide range of waveguide width and thickness due to further confined optical mode with higher index contrast.

4. H0-TYPE PHC CAVITY INTEGRATION

Among a variety of PhC cavities, we choose an H0-type cavity (also referred to as a "zero-cell" cavity or "point-shift" cavity) due to the ultrasmall mode volume and ease of integration with nanowire detectors. As shown in Figs. 5(a) and 5(b), the cavity is formed by slightly shifting two air holes away from their original positions by s in the direction of Γ-K in a 2D hexagonal lattice PhC. Following the previous discussions, we use a fully suspended slab made from material of 3.45 index for the PhC cavity design, while the thickness of the slab is chosen to be

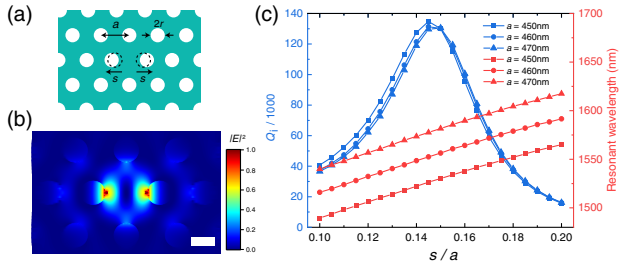

Fig. 5. H0-type PhC cavity design and optimization. (a) Schematic illustration of the H0-type PhC cavity formed by slightly shifting two air holes away from their original positions. a, r, and s denote the lattice constant, hole radius, and the amount of hole shifts, respectively. (b) Simulated electric field distribution of the H0-type PhC cavity at the resonant wavelength; scale bar, 200 nm. (c) Simulated intrinsic quality factor Q_i and resonant wavelength of the H0-type PhC cavity versus s/a for varying value of a.

220 nm, which is thicker than the optimal value shown in Fig. 4(f), considering the trade-off between the large-enough bandgap of the PhC and the strong evanescent field at the top surface, where the nanowire is situated.

We first start the optimization of the cavity from a lattice constant a of 480 nm to place the center of the bandgap at 1550 nm wavelength. Then, by iteratively tuning a, s (shift amount), and r (radii of the air holes), the best intrinsic quality factor Q_i is obtained with $r = 0.25a$. As shown in Fig. 5(c), the resonant wavelength increases with s and a, while the highest Q_i always occurs around $s = 0.15a$ independent of a. The decoupled Q_i from a allows us to adjust the resonance of the cavity to the target wavelength by freely tuning a. We choose $a = 455$ nm for the resonant wavelength of 1550 nm, and a Q_i of 132,000 combined with an ultrasmall mode volume of $0.22(\lambda/n)^3$ is achieved by 3D finite-difference time-domain (FDTD) simulation.

Based on the optimized design of the cavity, we simulate the coupling quality factor (Q_c) and the absorption quality factor (Q_a) by either making a partially reflective mirror for the cavity [Fig. 6(a)] or placing an NbN nanowire in the full cavity [Fig. 6(b)]. In Fig. 6(a), a W1-type PhC waveguide is formed by removing a row of the holes at the left side of the cavity, and a front partial mirror is inserted in between to couple the waveguide to the cavity. The reflectivity of the mirror or the coupling strength could be tuned by changing the number and the radii of the coupling holes making up the mirror. As shown in Fig. 6(b), the NbN nanowire detector comprises 2 of 120 deg arcs placed atop the slab and adjacent to the inner edges of the two shifted holes forming the cavity. The thickness, width, radius, and total length of the nanowire arcs are 5 nm, 80 nm, 265 nm, and 1.1 μm, respectively. The closest gap between the nanowire and the hole is set to 30 nm, considering a typical alignment tolerance in electron-beam exposure process. Figure 6(c) shows the simulated Q_a along with Q_c, depending on the number and radii of the coupling holes. With the nanowire loaded as a strong absorber, the cavity shows substantially reduced quality factor ($Q \approx Q_a = 39.8$), in sharp contrast to its Q_i. We could obtain near-unity absorption for the nanowire by engineering Q_c and fulfilling the critical coupling condition [$Q_c = Q_a$, equivalent to $|r| = \alpha$ in Fig. 1(a)]. As can be seen in Fig. 6(c), the matching condition requires two coupling holes and the optimal hole radius to be approximately 65 nm.

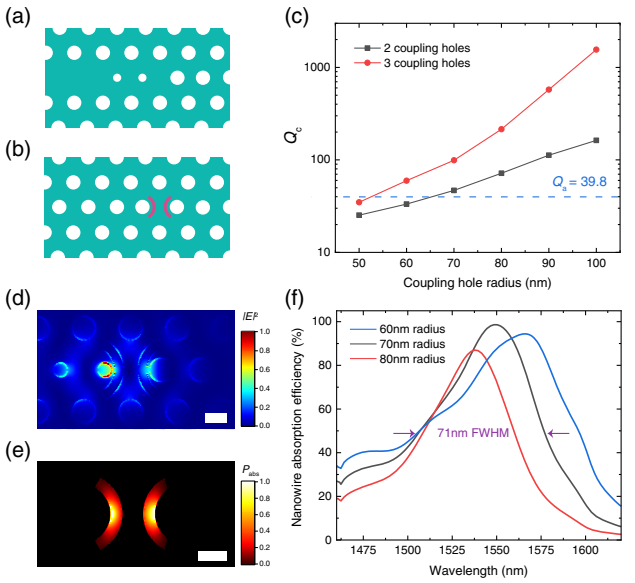

Fig. 6. Nanowire absorber integrated with H0-type PhC cavity. (a) Schematic of the H0-type PhC cavity with front partial mirror consisting of two smaller air holes. (b) Schematic of the H0-type PhC cavity with two arc-shaped nanowires embedded inside. (c) Simulated coupling quality factor Q_c of the H0-type PhC cavity as a function of the number and the radius of the coupling holes. The blue dashed line represents the absorption quality factor Q_a of the cavity with the nanowires loaded. (d) Simulated electric field distribution of the critically coupled H0-type PhC cavity at the resonant wavelength. (e) Simulated power dissipation density in the nanowires at the resonant wavelength. (f) Simulated dependence of the nanowire absorption on the wavelength for varying coupling hole sizes. The FWHM defining the 3 dB bandwidth of the nanowire detector at the critical coupling condition is marked by a pair of purple arrows; all scale bars, 200 nm.

In order to further investigate the maximum absorption and the frequency response of the nanowire-cavity system, we excite a propagating mode in the coupling PhC waveguide and simulate the absorption by the nanowire as a function of the wavelength around 1550 nm. As shown in Figs. 6(d) and 6(e), the electric field is strongly confined at the inner edges of the shifted holes, resulting in greatly enhanced power absorption at the center of the nanowire arcs. We note that the electric field and thus the absorption at the ends of the nanowire arcs are very weak, and therefore the nanowires could be quickly tapered to much thicker wires for the electrical connection without introducing much extra absorption in the photon-insensitive area. Figure 6(f) shows the wavelength-dependent nanowire absorption efficiency normalized to the incident power carried by the coupling waveguide. As the size of coupling holes increases, we could clearly see the transition from overcoupling ($Q_c < Q_a$) to undercoupling ($Q_c > Q_a$). The critical coupling condition is fulfilled with two 70 nm-radius holes, and the maximum absorption efficiency of 98.6% is recorded at 1549.6 nm. We attribute the remaining photon loss to the scattering, which could be further reduced by structure optimization, such as individual tuning of the two coupling hole sizes and positions. From the numerically simulated spectrum, the FWHM or 3 dB bandwidth at the critical coupling condition is 71 nm, corresponding to a overall loaded quality factor $Q_l = 21.8$, which is in good agreement with the prediction results by the method of quality-factor matching [Fig. 6(c)], where $Q_l = (Q_a^{-1} + Q_c^{-1})^{-1} = Q_a/2 = 19.9$.

5. DISCUSSION AND CONCLUSION

There is a general trade-off in all cavity-integrated perfect absorber design between the absorption volume and the absorption bandwidth, as derived from Eq. (6). For example, for less absorption volume (smaller α) or shorter nanowires in the case of cavity-integrated SNSPDs, the photons are expected to experience more round trips inside the cavity to achieve a near-unity absorption, which entails higher finesse of the cavity (larger Q_l for the fixed cavity mode volume) at the expense of

Table 1. Summary and Comparison of SNSPDs with Different Device Structures

Reference	Device Type	Nanowire Length (μm)	3 dB Bandwidth (nm)	Figure of Merit F ($\times 10^{-3}$)
Ref. [38]	Meander nanowire + vertical cavity + metal mirror	1150	700	0.6
Ref. [7]	Meander nanowire + vertical cavity + distributed Bragg reflector (DBR) mirror	1350	400	0.3
Ref. [54]	Microfiber-coupled meander nanowire	1100	870	0.8
Ref. [35]	Racetrack resonator integration	1	1	1
Ref. [34]	1D PhC cavity integration	8.5	5.6	0.7
Ref. [32]	1D PhC cavity integration	1	10	10
Ref. [12]	2D PhC cavity integration	3	13.2	4.4
This work	H0-type PhC cavity integration	1.1	71	64.5

reduced bandwidth. Therefore, we introduce a figure of merit defined as bandwidth-nanowire-length ratio $F = B/\mathrm{NL}$ to balance the design compromise between B and NL, where NL is the length of the nanowire required for achieving near-unity maximum absorption, and B stands for the 3 dB bandwidth of the nanowire absorption spectrum. Table 1 shows the comparison of our work in terms of B, NL, and F with other types of recently demonstrated SNSPDs, including meander-type detectors integrated with vertical cavities, detectors integrated with waveguides, and various types of on-chip cavities. In comparison with traditional meander-type SNSPDs, our H0-type 2D PhC cavity design shows 2 orders of magnitude improved $F = 64.5$, with a dramatically reduced nanowire length down to 1.1 μm. In the meanwhile, this design still maintains a significantly enhanced 3 dB bandwidth of 71 nm, compared to other cavity-integrated SNSPDs.

It is worth noting that although we use the NbN thin film as the material of the superconducting nanowire, our proposed design is also compatible with other superconducting materials, such as WSi [6] and MoSi [55,56], which have been made into high-efficiency SNSPDs recently. It should also be mentioned that the fully suspended HIC waveguide that our designs are based on could be realized either on Si or GaAs platforms, which benefits the realization of photonic circuits in very compact size. In particular, GaAs has drawn great research interest recently due to its strong $\chi^{(2)}$ and $\chi^{(3)}$ nonlinearity [48], large electro-optic effect [57], as well as the capability of on-chip single-photon detector integration [25] and quantum dot growth as on-demand single-photon sources [58]. These excellent optical functionalities render GaAs a very promising candidate platform for realizing fully integrated quantum photonic circuits with the generation, routing, active manipulation, and the final detection of single photons on a single chip [58,59].

Combined, we expect that our proposed design will enable a large array of high-performance on-chip single-photon detectors for future integrated quantum photonic circuits, simultaneously offering high efficiency, large bandwidth, ultralow jitter, ultrafast gigahertz counting rates, as well as high fabrication yield.

Funding. Army Research Office (W911NF-16-2-0151); Division of Emerging Frontiers in Research and Innovation (EFMA-1640959); Multidisciplinary University Research Initiative (FA95550-15-1-0029).

Acknowledgment. We thank Dr. Xiang Guo and Dr. Linran Fan for the fruitful discussions.

Disclosures. The authors declare no conflicts of interest.

REFERENCES

1. G. Gol'Tsman, O. Okunev, G. Chulkova, A. Lipatov, A. Semenov, K. Smirnov, B. Voronov, A. Dzardanov, C. Williams, and R. Sobolewski, "Picosecond superconducting single-photon optical detector," Appl. Phys. Lett. **79**, 705–707 (2001).
2. R. H. Hadfield, "Single-photon detectors for optical quantum information applications," Nat. Photonics **3**, 696–705 (2009).
3. H. Takesue, S. W. Nam, Q. Zhang, R. H. Hadfield, T. Honjo, K. Tamaki, and Y. Yamamoto, "Quantum key distribution over a 40-dB channel loss using superconducting single-photon detectors," Nat. Photonics **1**, 343–348 (2007).
4. J. Wang, S. Paesani, Y. Ding, R. Santagati, P. Skrzypczyk, A. Salavrakos, J. Tura, R. Augusiak, L. Mančinska, D. Bacco, and D. Bonneau, "Multidimensional quantum entanglement with large-scale integrated optics," Science **360**, 285–291 (2018).
5. S.-K. Liao, W.-Q. Cai, W.-Y. Liu, L. Zhang, Y. Li, J.-G. Ren, J. Yin, Q. Shen, Y. Cao, Z.-P. Li, and F. Z. Li, "Satellite-to-ground quantum key distribution," Nature **549**, 43–47 (2017).
6. F. Marsili, V. B. Verma, J. A. Stern, S. Harrington, A. E. Lita, T. Gerrits, I. Vayshenker, B. Baek, M. D. Shaw, R. P. Mirin, and S. W. Nam, "Detecting single infrared photons with 93% system efficiency," Nat. Photonics **7**, 210–214 (2013).
7. W. Zhang, L. You, H. Li, J. Huang, C. Lv, L. Zhang, X. Liu, J. Wu, Z. Wang, and X. Xie, "NbN superconducting nanowire single photon detector with efficiency over 90% at 1550 nm wavelength operational at compact cryocooler temperature," Sci. China Phys. Mech. Astron. **60**, 120314 (2017).
8. I. Esmaeil Zadeh, J. W. Los, R. B. Gourgues, V. Steinmetz, G. Bulgarini, S. M. Dobrovolskiy, V. Zwiller, and S. N. Dorenbos, "Single-photon detectors combining high efficiency, high detection rates, and ultra-high timing resolution," APL Photon. **2**, 111301 (2017).
9. V. Verma, A. Lita, B. Korzh, E. Wollman, M. Shaw, R. Mirin, and S. Nam, "Towards single-photon spectroscopy in the mid-infrared using superconducting nanowire single-photon detectors," Proc. SPIE **10978**, 109780N (2019).
10. F. Marsili, F. Bellei, F. Najafi, A. E. Dane, E. A. Dauler, R. J. Molnar, and K. K. Berggren, "Efficient single photon detection from 500 nm to 5 μm wavelength," Nano Lett. **12**, 4799–4804 (2012).
11. R. Cheng, C.-L. Zou, X. Guo, S. Wang, X. Han, and H. X. Tang, "Broadband on-chip single-photon spectrometer," Nat. Commun. **10**, 1 (2019).
12. J. Münzberg, A. Vetter, F. Beutel, W. Hartmann, S. Ferrari, W. H. Pernice, and C. Rockstuhl, "Superconducting nanowire single-photon detector implemented in a 2D photonic crystal cavity," Optica **5**, 658–665 (2018).
13. W. Zhang, J. Huang, C. Zhang, L. You, C. Lv, L. Zhang, H. Li, Z. Wang, and X. Xie, "A 16-pixel interleaved superconducting nanowire

single-photon detector array with a maximum count rate exceeding 1.5 GHz," IEEE Trans. Appl. Supercond. **29**, 2200204 (2019).
14. I. E. Zadeh, J. W. Los, R. Gourgues, G. Bulgarini, S. M. Dobrovolskiy, V. Zwiller, and S. N. Dorenbos, "A single-photon detector with high efficiency and sub-10 ps time resolution," arXiv:1801.06574 (2018).
15. M. Caloz, B. Korzh, E. Ramirez, C. Schönenberger, R. J. Warburton, H. Zbinden, M. D. Shaw, and F. Bussières, "Intrinsically-limited timing jitter in molybdenum silicide superconducting nanowire single-photon detectors," arXiv:1906.02073 (2019).
16. B. Korzh, Q.-Y. Zhao, J. P. Allmaras, S. Frasca, T. M. Autry, E. A. Bersin, A. D. Beyer, R. M. Briggs, B. Bumble, M. Colangelo, G. M. Crouch, A. E. Dane, T. Gerrits, A. E. Lita, F. Marsili, G. Moody, C. Peña, E. Ramirez, J. D. Rezac, N. Sinclair, M. J. Stevens, A. E. Velasco, V. B. Verma, E. E. Wollman, S. Xie, D. Zhu, P. D. Hale, M. Spiropulu, K. L. Silverman, R. P. Mirin, S. W. Nam, A. G. Kozorezov, M. D. Shaw, and K. K. Berggren, "Demonstration of sub-3 ps temporal resolution with a superconducting nanowire single-photon detector," Nat. Photonics **14**, 250–255 (2020).
17. C. Schuck, W. H. Pernice, and H. X. Tang, "Waveguide integrated low noise NbTiN nanowire single-photon detectors with milli-Hz dark count rate," Sci. Rep. **3**, 1893 (2013).
18. H. Shibata, K. Shimizu, H. Takesue, and Y. Tokura, "Ultimate low system dark-count rate for superconducting nanowire single-photon detector," Opt. Lett. **40**, 3428–3431 (2015).
19. R. Cheng, M. Poot, X. Guo, L. Fan, and H. X. Tang, "Large-area superconducting nanowire single-photon detector with double-stage avalanche structure," IEEE Trans. Appl. Supercond. **27**, 2200805 (2017).
20. A. J. Kerman, E. A. Dauler, W. E. Keicher, J. K. Yang, K. K. Berggren, G. Gol'Tsman, and B. Voronov, "Kinetic-inductance-limited reset time of superconducting nanowire photon counters," Appl. Phys. Lett. **88**, 111116 (2006).
21. J. P. Sprengers, A. Gaggero, D. Sahin, S. Jahanmirinejad, G. Frucci, F. Mattioli, R. Leoni, J. Beetz, M. Lermer, M. Kamp, S. Höfling, R. Sanjines, and A. Fiore, "Waveguide superconducting single-photon detectors for integrated quantum photonic circuits," Appl. Phys. Lett. **99**, 181110 (2011).
22. W. H. Pernice, C. Schuck, O. Minaeva, M. Li, G. Goltsman, A. Sergienko, and H. Tang, "High-speed and high-efficiency travelling wave single-photon detectors embedded in nanophotonic circuits," Nat. Commun. **3**, 1325 (2012).
23. C. Schuck, W. H. P. Pernice, and H. X. Tang, "NbTiN superconducting nanowire detectors for visible and telecom wavelengths single photon counting on Si_3N_4 photonic circuits," Appl. Phys. Lett. **102**, 051101 (2013).
24. V. Kovalyuk, W. Hartmann, O. Kahl, N. Kaurova, A. Korneev, G. Goltsman, and W. Pernice, "Absorption engineering of NbN nanowires deposited on silicon nitride nanophotonic circuits," Opt. Express **21**, 22683–22692 (2013).
25. D. Sahin, A. Gaggero, J.-W. Weber, I. Agafonov, M. A. Verheijen, F. Mattioli, J. Beetz, M. Kamp, S. Höfling, M. C. van de Sanden, and R. Leoni, "Waveguide nanowire superconducting single-photon detectors fabricated on GaAs and the study of their optical properties," IEEE J. Sel. Top. Quantum Electron. **21**, 3800210 (2015).
26. O. Kahl, S. Ferrari, V. Kovalyuk, G. N. Goltsman, A. Korneev, and W. H. Pernice, "Waveguide integrated superconducting single-photon detectors with high internal quantum efficiency at telecom wavelengths," Sci. Rep. **5**, 10941 (2015).
27. P. Rath, O. Kahl, S. Ferrari, F. Sproll, G. Lewes-Malandrakis, D. Brink, K. Ilin, M. Siegel, C. Nebel, and W. Pernice, "Superconducting single-photon detectors integrated with diamond nanophotonic circuits," Light: Sci. Appl. **4**, e338 (2015).
28. F. Najafi, J. Mower, N. C. Harris, F. Bellei, A. Dane, C. Lee, X. Hu, P. Kharel, F. Marsili, S. Assefa, and K. K. Berggren, "On-chip detection of non-classical light by scalable integration of single-photon detectors," Nat. Commun. **6**, 5873 (2015).
29. J. Li, R. A. Kirkwood, L. J. Baker, D. Bosworth, K. Erotokritou, A. Banerjee, R. M. Heath, C. M. Natarajan, Z. H. Barber, M. Sorel, and R. H. Hadfield, "Nano-optical single-photon response mapping of waveguide integrated molybdenum silicide (MoSi) superconducting nanowires," Opt. Express **24**, 13931–13938 (2016).
30. S. Ferrari, C. Schuck, and W. Pernice, "Waveguide-integrated superconducting nanowire single-photon detectors," Nanophotonics **7**, 1725–1758 (2018).
31. A. Gaggero, F. Martini, F. Mattioli, F. Chiarello, R. Cernansky, A. Politi, and R. Leoni, "Amplitude-multiplexed readout of single photon detectors based on superconducting nanowires," Optica **6**, 823–828 (2019).
32. A. Vetter, S. Ferrari, P. Rath, R. Alaee, O. Kahl, V. Kovalyuk, S. Diewald, G. N. Goltsman, A. Korneev, C. Rockstuhl, and W. H. Pernice, "Cavity-enhanced and ultrafast superconducting single-photon detectors," Nano Lett. **16**, 7085–7092 (2016).
33. N. Calandri, Q.-Y. Zhao, D. Zhu, A. Dane, and K. K. Berggren, "Superconducting nanowire detector jitter limited by detector geometry," Appl. Phys. Lett. **109**, 152601 (2016).
34. M. K. Akhlaghi, E. Schelew, and J. F. Young, "Waveguide integrated superconducting single-photon detectors implemented as near-perfect absorbers of coherent radiation," Nat. Commun. **6**, 8233 (2015).
35. N. A. Tyler, J. Barreto, G. E. Villarreal-Garcia, D. Bonneau, D. Sahin, J. L. O'Brien, and M. G. Thompson, "Modelling superconducting nanowire single photon detectors in a waveguide cavity," Opt. Express **24**, 8797–8808 (2016).
36. M. Born and E. Wolf, *Principles of Optics: Electromagnetic Theory of Propagation, Interference and Diffraction of Light* (Elsevier, 2013).
37. A. Yariv, "Critical coupling and its control in optical waveguide-ring resonator systems," IEEE Photon. Technol. Lett. **14**, 483–485 (2002).
38. Y. Wang, H. Li, L. You, C. Lv, J. Huang, W. Zhang, L. Zhang, X. Liu, Z. Wang, and X. Xie, "Broadband near-infrared superconducting nanowire single-photon detector with efficiency over 50%," IEEE Trans. Appl. Supercond. **27**, 2200904 (2016).
39. W. Bogaerts, P. D. Heyn, T. V. Vaerenbergh, K. D. Vos, S. K. Selvaraja, T. Claes, P. Dumon, P. Bienstman, D. V. Thourhout, and R. Baets, "Silicon microring resonators," Laser Photon. Rev. **6**, 47–73 (2011).
40. X. Guo, C.-L. Zou, C. Schuck, H. Jung, R. Cheng, and H. X. Tang, "Parametric down-conversion photon-pair source on a nanophotonic chip," Light: Sci. Appl. **6**, e16249 (2017).
41. L. Fan, C.-L. Zou, R. Cheng, X. Guo, X. Han, Z. Gong, S. Wang, and H. X. Tang, "Superconducting cavity electro-optics: a platform for coherent photon conversion between superconducting and photonic circuits," Sci. Adv. **4**, eaar4994 (2018).
42. E. Yablonovitch, "Inhibited spontaneous emission in solid-state physics and electronics," Phys. Rev. Lett. **58**, 2059–2062 (1987).
43. Y. Akahane, T. Asano, B.-S. Song, and S. Noda, "High-Q photonic nanocavity in a two-dimensional photonic crystal," Nature **425**, 944–947 (2003).
44. C. Xiong, W. Pernice, K. K. Ryu, C. Schuck, K. Y. Fong, T. Palacios, and H. X. Tang, "Integrated GaN photonic circuits on silicon (100) for second harmonic generation," Opt. Express **19**, 10462–10470 (2011).
45. C. Xiong, W. H. Pernice, X. Sun, C. Schuck, K. Y. Fong, and H. X. Tang, "Aluminum nitride as a new material for chip-scale optomechanics and nonlinear optics," New J. Phys. **14**, 095014 (2012).
46. C. Wang, M. Zhang, X. Chen, M. Bertrand, A. Shams-Ansari, S. Chandrasekhar, P. Winzer, and M. Lončar, "Integrated lithium niobate electro-optic modulators operating at CMOS-compatible voltages," Nature **562**, 101–104 (2018).
47. A. A. Sayem, R. Cheng, S. Wang, and H. X. Tang, "Lithium-niobate-on-insulator waveguide-integrated superconducting nanowire single-photon detectors," arXiv:1912.09418 (2019).
48. L. Chang, A. Boes, X. Guo, D. T. Spencer, M. Kennedy, J. D. Peters, N. Volet, J. Chiles, A. Kowligy, N. Nader, and D. D. Hickstein, "Heterogeneously integrated GaAs waveguides on insulator for efficient frequency conversion," Laser Photon. Rev. **12**, 1800149 (2018).
49. V. Anant, A. J. Kerman, E. A. Dauler, J. K. Yang, K. M. Rosfjord, and K. K. Berggren, "Optical properties of superconducting nanowire single-photon detectors," Opt. Express **16**, 10750–10761 (2008).
50. R. Cheng, S. Wang, and H. X. Tang, "Superconducting nanowire single-photon detectors fabricated from atomic-layer-deposited NbN," Appl. Phys. Lett. **115**, 241101 (2019).

51. J. R. Clem and K. K. Berggren, "Geometry-dependent critical currents in superconducting nanocircuits," Phys. Rev. B **84**, 174510 (2011).
52. Q. Guo, H. Li, L. You, W. Zhang, L. Zhang, Z. Wang, X. Xie, and M. Qi, "Single photon detector with high polarization sensitivity," Sci. Rep. **5**, 9616 (2015).
53. S. Miki, M. Yabuno, T. Yamashita, and H. Terai, "Stable, high-performance operation of a fiber-coupled superconducting nanowire avalanche photon detector," Opt. Express **25**, 6796–6804 (2017).
54. X. Hou, N. Yao, L. You, H. Li, Y. Wang, W. Zhang, H. Wang, X. Liu, W. Fang, L. Tong, Z. Wang, and X. Xie, "Ultra-broadband microfiber-coupled superconducting single-photon detector," Opt. Express **27**, 25241–25250 (2019).
55. D. V. Reddy, A. E. Lita, S. W. Nam, R. P. Mirin, and V. B. Verma, "Achieving 98% system efficiency at 1550 nm in superconducting nanowire single photon detectors," in *Rochester Conference on Coherence and Quantum Optics (CQO-11)* (OSA, 2019), paper W2B.2.
56. M. Caloz, M. Perrenoud, C. Autebert, B. Korzh, M. Weiss, C. Schönenberger, R. J. Warburton, H. Zbinden, and F. Bussières, "High-detection efficiency and low-timing jitter with amorphous superconducting nanowire single-photon detectors," Appl. Phys. Lett. **112**, 061103 (2018).
57. J. Wang, A. Santamato, P. Jiang, D. Bonneau, E. Engin, J. W. Silverstone, M. Lermer, J. Beetz, M. Kamp, S. Höfling, and M. G. Tanner, "Gallium arsenide (GaAs) quantum photonic waveguide circuits," Opt. Commun. **327**, 49–55 (2014).
58. C. P. Dietrich, A. Fiore, M. G. Thompson, M. Kamp, and S. Höfling, "GaAs integrated quantum photonics: towards compact and multi-functional quantum photonic integrated circuits," Laser Photon. Rev. **10**, 870–894 (2016).
59. M. Schwartz, E. Schmidt, U. Rengstl, F. Hornung, S. Hepp, S. L. Portalupi, K. Ilin, M. Jetter, M. Siegel, and P. Michler, "Fully on-chip single-photon Hanbury-Brown and Twiss experiment on a monolithic semiconductor-superconductor platform," Nano Lett. **18**, 6892–6897 (2018).